Development of an in-situ laser calibration method for multi-laser powder bed fusion additive manufacturing system

Ho Yeung[1], David Deisenroth, Sergey Mekhontsev
National Institute of Standards and Technology, Gaithersburg, MD 20899

Abstract

A new in-situ laser calibration method for multi-laser powder bed fusion (L-PBF) systems has been developed to address the prevalent challenges of part quality at the stitched regions due to misalignments of different lasers. In the proposed method, cameras coaxially aligned with the processing lasers are utilized, capturing images of a dimensional reference artifact during scanning and reconstructing the scan path from these images in the artifact's coordinates. This enables an automated and precise calibration of each laser to a unified global coordinate system without the necessity of external measurements. Preliminary tests show that the patterns scanned by two different laser systems are highly superimposed, with errors less than 20 micrometers. This method is expected to enhance the efficiency and quality of multi-laser L-PBF systems by ensuring precise alignment and synchronization of laser beams.

Introduction

The metal Laser Powder Bed Fusion (L-PBF) process is one of the most widely used metal additive manufacturing techniques. It enables the creation of complex features, optimized geometries, lightweight components, and intricate designs [1]. However, the widespread adoption of this technology is hindered by two significant factors: productivity and part quality. The L-PBF process builds parts layer by layer by melting and solidifying cross-sectional shapes of the part from freshly spread metal powder layers using a high-energy scanning laser beam. Theoretically, productivity can be enhanced by employing multiple laser beams that scan simultaneously, with intelligent stitching of the scanning regions. However, recent studies have shown that defects such as surface quality degradation, internal gaseous pores, and lack of fusion are more likely to occur in the stitched regions of parts fabricated by multi-laser systems [2,3]. A potential cause of these quality issues is the laser position error over the stitched regions [4], leading to gaps or overlaps due to inadequate galvo calibration, resulting in lack of fusion, laser intersection, and overheating.

In a typical L-PBF machine, the laser is guided to the build plane by a pair of mirrors driven at high speeds by galvo motors, forming an X-Y scan coordinate system. Therefore, laser position calibration is effectively equivalent to the galvo calibration, and these terms are used interchangeably in this paper. For multiple lasers to work on a single part, the individual coordinate systems must be calibrated and aligned to a single global machine coordinate system. Galvo calibration is usually performed by "burning" a pattern on a test plate and measuring its dimensions ex-situ [5,6], often referred to as "mark and measure" method. The uncertainties in this process

[1] Corresponding author, ho.yeung@nist.gov
Certain commercial equipment, instruments, or materials are identified in this paper in order to specify the experimental procedure adequately. Such identification is not intended to imply recommendation or endorsement by NIST, nor is it intended to imply that the materials or equipment identified are necessarily the best available for the purpose.

primarily arise from the non-repeatable burn features (due to the physical process of melting and solidification on the substrate) and errors in determining the locations of the marks. This method relies on external measurement, making it difficult to automate and prone to human error. An alternative approach involves placing sensors, such as an up-looking camera [7] or thermal-sensitive device [8], directly on the build plane to measure the laser position without burning. However, covering the entire build plane with high-resolution sensors is impractical due to the prohibitive cost. A possible solution is to mount the sensor on a high-precision motorized stage, allowing it to be positioned at various locations. However, this approach would make the calibration accuracy dependent on both the sensor resolution and the mechanical stage repeatability. Additionally, this external measurement approach cannot calibrate the temporal synchronization of multiple galvo systems, further limiting its effectiveness.

An in-situ laser calibration method for multi-laser L-PBF systems has been developed. This calibration method utilizes cameras coaxially aligned with the processing lasers, capturing images of a dimensional reference artifact (optical target) while scanning it with the galvo system following a programmed path. Figure 1 illustrates the concept, with 1a showing the coaxial imaging setup and 1b depicting a typical optical target, along with the coordinate systems defined by the optical target (T), camera (C), and galvo (G). Each individual laser has its own associated C and G coordinate systems. The captured image positions can be located within the T coordinate system by pattern matching a feature on the target. Because the processing laser and camera share the same optical path, the laser spot consistently appears at the same position in the coaxial camera's field of view, with a constant offset from the image center. The laser/galvo position is measured by identifying the image center position within T, making each image a calibration point. This process can be fully automated, enabling the collection of thousands of calibration points before the build, with in-process mapping applied to align all lasers to the same global coordinates in T. This method, first developed by Yeung et al [9] for a single laser system, achieved an average error ± standard deviation of 7.31 µm ± 5.32 µm in the x-direction and 5.25 µm ± 2.41 µm in the y-direction, using a coaxial camera with a resolution of 8 µm per pixel. This study will extend this method to a multi-laser system.

The adoption of multi-laser systems represents a future direction for the additive manufacturing (AM) industry. The proposed in-situ calibration method could significantly enhance the build quality of these multi-laser systems. By combining the spatial accuracy achieved through this calibration technique with the temporal accuracy provided by the jerk-limited galvo control that we developed in [10], multiple laser beams can work seamlessly together to implement more advanced scan strategies to build faster and better. These strategies include pre-sintering to reduce powder denudation, post-heating for residual stress relief, and creating unique heating conditions for microstructure control (intrinsic heat treatment) [11]. This approach has the potential to fully realize the benefits of multi-laser systems and significantly advance the AM industry.

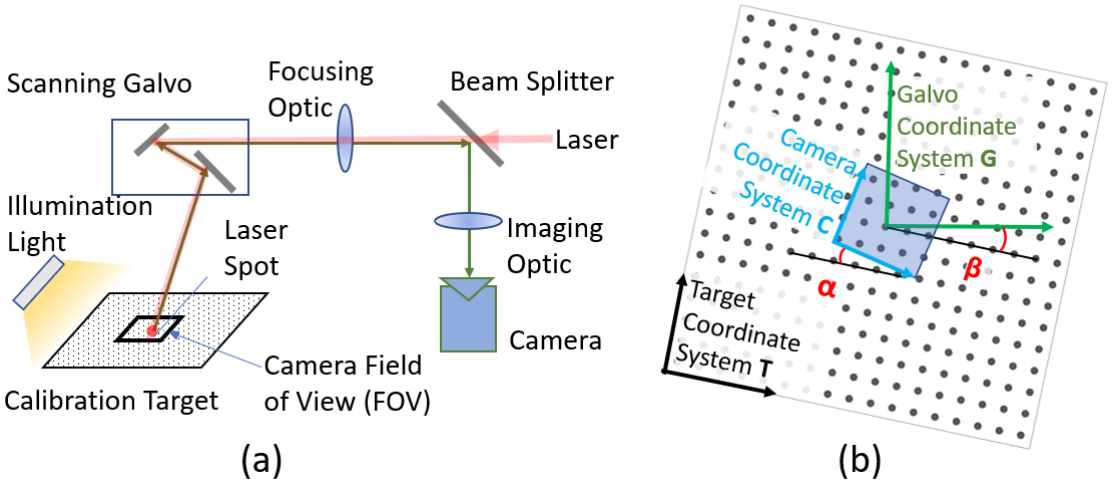

Figure 1. In-situ galvo spatial calibration. (a) Calibration set up. (b) Optical target, camera and galvo 2D alignment [9]

Galvo Calibration and Compensation Method

The calibration technique employs a camera coaxially aligned with a laser to image a dimensional reference artifact. Figure 2 shows a sample artifact consisting of 289 feature groups arranged in a 17 by 17 grid, with each group containing four concentric circles and five crosshair features organized in a 3 mm x 3 mm pattern. The A1 features within each group are used for position tracking. A scan path is designed to raster horizontally and upward in 0.467 mm steps, starting from the bottom left corner of the target. The scan is programmed to dwell at each step for 10 ms, with the camera triggered 1 ms after the scan stops, and an exposure time of 8 ms ensures that images are captured only when the galvo is stationary. A total of 7,872 images are taken, and digital image correlation (DIC) is used to trace the position markers, determining the image position within the optical reference. Because the camera and laser share the same optical path, this setup allows for precise determination of the laser's location, ensuring accurate calibration by correlating captured image positions to the laser's true location on the target.

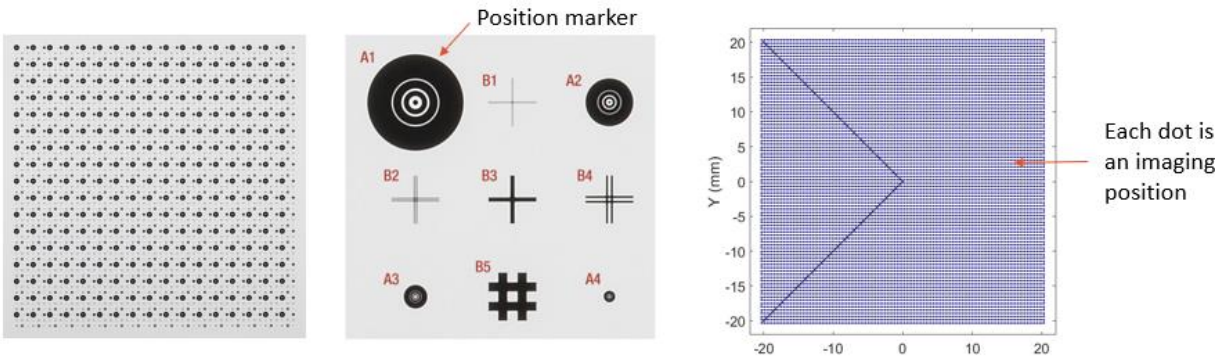

Figure 2. Commercial optical target used for dimensional reference (a) Entire target consists of 289 feature groups of 3 mm x 3 mm each. (b) Close up of a group, where feature A1 is used as the marker for position detection. (c) Scan path raster through the optical target.

As a result, a measured path can be reconstructed in the optic reference coordinates and is plotted in Figure 3 alongside the commanded path. These two paths can be represented by two X-Y position arrays: the XY command array (XYC) and the corresponding measured position array (XYT). The position error is calculated as XYC – XYT. Polynomials can be fitted to map XYC to XYT, which is noted as *sf_c2t*, representing the machine position model. The transfer function from XYT to XYC, denoted as *sf_t2c*, serves as the compensation function to correct the machine's position error. Theoretically, if a function *sf_t2c* can be identified such that *sf_t2c*(XYT) – XYC = 0, then the machine's position error can be completely eliminated by applying *sf_t2c* to XYC before execution on the machine. In other words, *sf_t2c*(XYC) is the compensated command, and its execution can be represented as *sf_c2t*(*sf_t2c*(XYC)) = XYC = XYT, as illustrated in Figure 3. In non-ideal cases, *sf_t2c*(XYT) – XYC can be referred to as the compensation error, indicating how effectively the machine's position error is corrected. It is crucial to identify the correct compensation function *sf_t2c* to minimize the compensation error. Table 1 summarizes the acronyms and symbols used above.

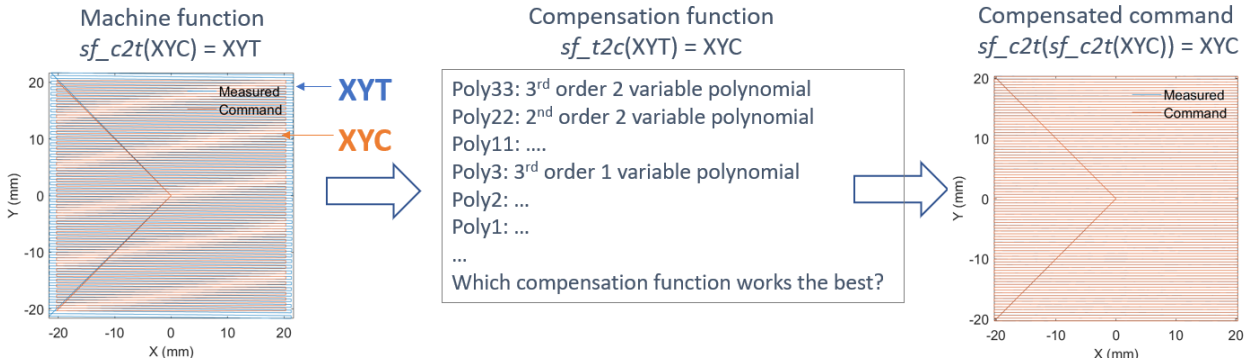

Figure 3. The figure illustrates how the machine position error is compensated.

Table 1. Acronyms and symbols

Acronym/Symbol	Definition
XYC	X-Y Command array representing the intended position coordinates.
XYT	X-Y Measured array representing the measured position coordinates.
XYC – XYT	Position error, calculated as the difference between the commanded position (XYC) and the measured position (XYT).
sf_c2t	Machine position model function that maps the XYC (commanded position) to XYT (measured position).
sf_t2c	Compensation function that maps XYT (measured position) to XYC (commanded position) to correct the machine's position error.
sf_t2c(XYT) – XYC	Compensation error, indicating the difference between the corrected position and the intended command position, used to evaluate the effectiveness of the compensation function.
sf_c2t(*sf_t2c*(XYC))	Represents the application of the compensation function to the command position, with the goal of achieving the desired position after correction, ideally resulting in the equation XYT = XYC.

The National Institute of Standards and Technology (NIST) has developed a unique approach to laser control known as pointwise control [12], which uses a time-stepped digital command build file executed by the controller implemented with Field Programmable Gate Array (FPGA) technology. The compensation function can be applied directly to the build file. This is shown in Figure 4. However, a more logical approach is to make the compensation in the controller in real-time during execution. While this method simplifies scan file preparation, it is constrained by the real-time computing resources available; therefore, higher order compensation which requires longer computing time may not be feasible. In this study, both approaches—pre-compensation and real-time compensation—are tested.

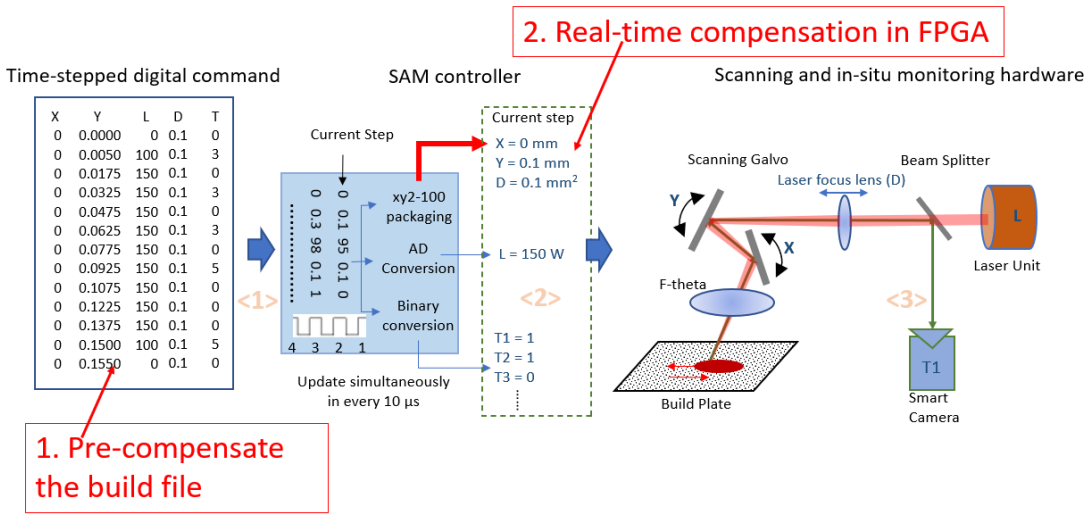

Figure 4. Integration of laser position compensation into the L-PBF control system.

Figure 5 shows the user interface for an in-house developed dual laser AM controller, known as the Simple AM (SAM) controller, implemented in LabVIEW within the National Instruments (NI) Compact RIO system. The SAM dual laser controller is designed to enable effective collaboration between the two lasers during the build process. The system offers multiple operation modes, including: synchronized mode, where both lasers execute the same command file simultaneously; lead/follow mode, where one laser leads the other by a predefined time; and parallel mode, where one laser offsets the other by a predefined distance. The goal of this dual laser system is not only to increase build speed but also to achieve better control over the local temperature history. For this study, the synchronized mode was applied to drive two lasers simultaneously to scan though the same XYC coordinates.

The current SAM dual laser controller allows each laser to be compensated in real-time independently by applying a second-order single-variable polynomial (poly2) in the format of $ax^2 + bx + c$ to each axis. This approach assumes no cross-axis interference. While higher-order two-variable polynomials could be developed to address cross-axis interference, these may be constrained by available hardware resources and processing speed. Therefore, from a system implementation perspective, it is crucial to determine the appropriate level of correction needed to achieve the desired accuracy.

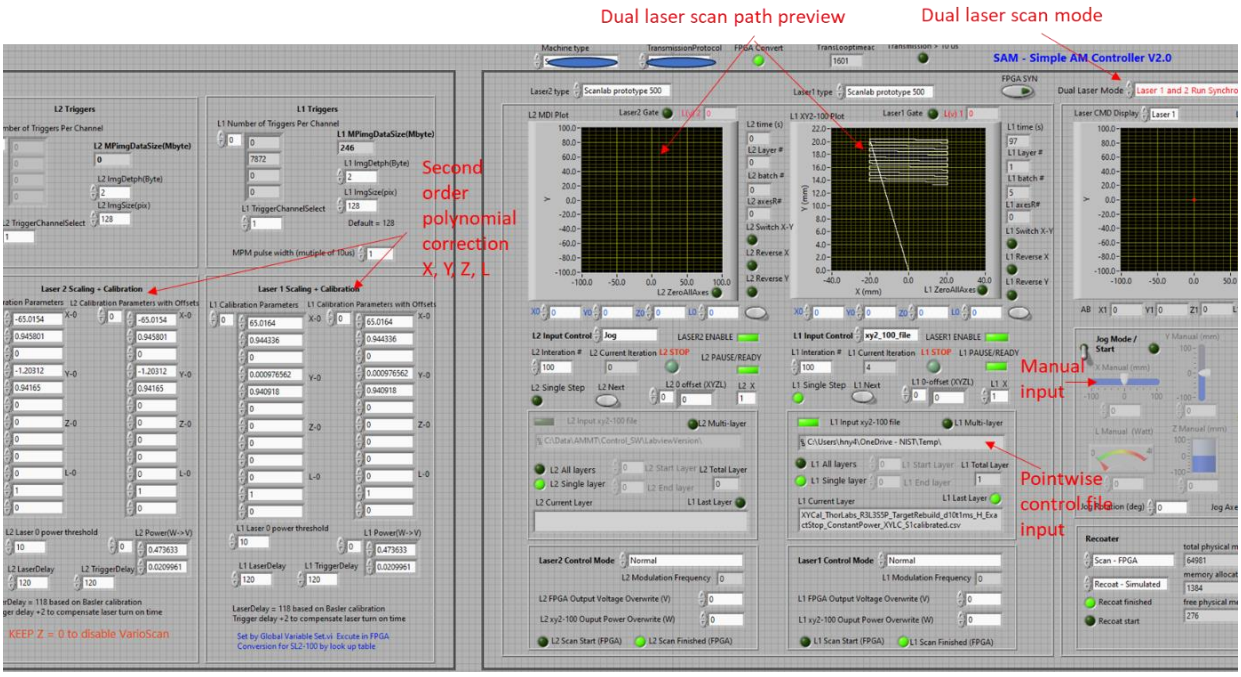

Figure 5. SAM dual laser controller interface. The SAM system allows users to input a second-order polynomial for position compensation for each of the x and y axis for both galvo systems. This compensation is executed in real-time in FPGA.

Experiments

The calibration experiment was conducted on the NIST Additive Manufacturing Metrology Testbed (AMMT) 2.0 prototype system, as shown in Figure 6. The prototype is driven by the SAM controller. The scan file depicted in Figure 2c was executed on both galvos simultaneously, with the two coaxial cameras triggered to capture images at the same time. Because both lasers are calibrated using the same optical reference, it is logical to place this reference approximately at the center of the two scanners, as shown in Figure 7. The guide beams of the lasers were then positioned at the same center marker on the optical target. During this process, the galvos were positioned near the center of the optical target by observing the guide beam, with Galvo A at (65, 0) mm and Galvo B at (-65, -1.5) mm. These offsets were set in the SAM controllers, offsetting the origins G1 and G2 to these positions. Because the algorithm uses the center of the position marker (C1 and C2) as the origin, their relative positions are also noted and used as the offset between the two galvos. However, this is done after the image is corrected for orientation and restoration, as explained in [9]. As a result, the entire process does not require high-precision positioning and is relatively easy to set up.

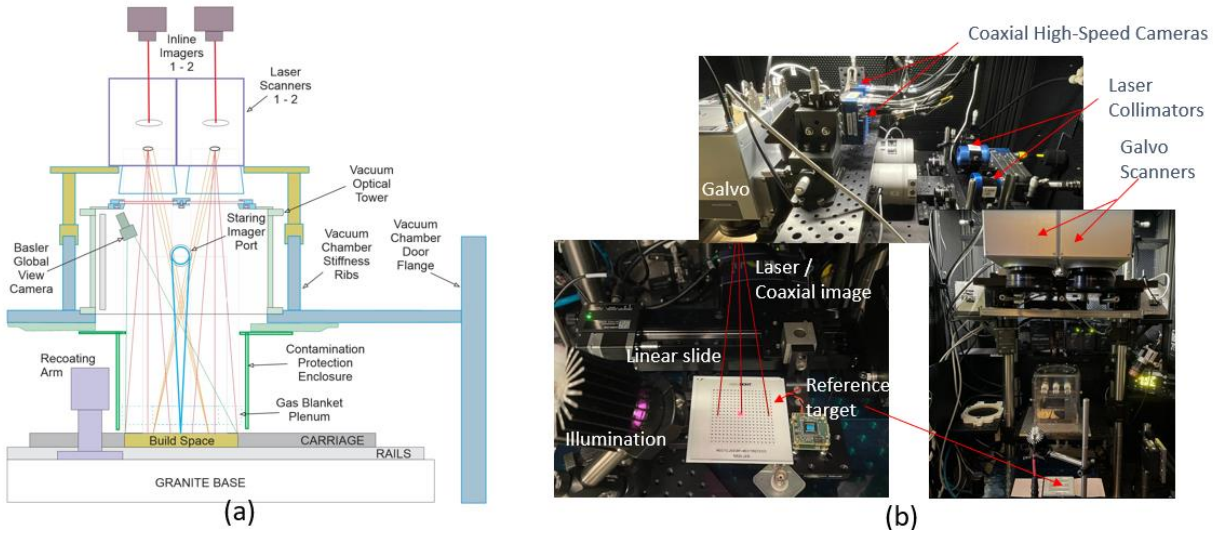

Figure 6. Experiment setup (a) Schematic (b) Picture of the dual laser system.

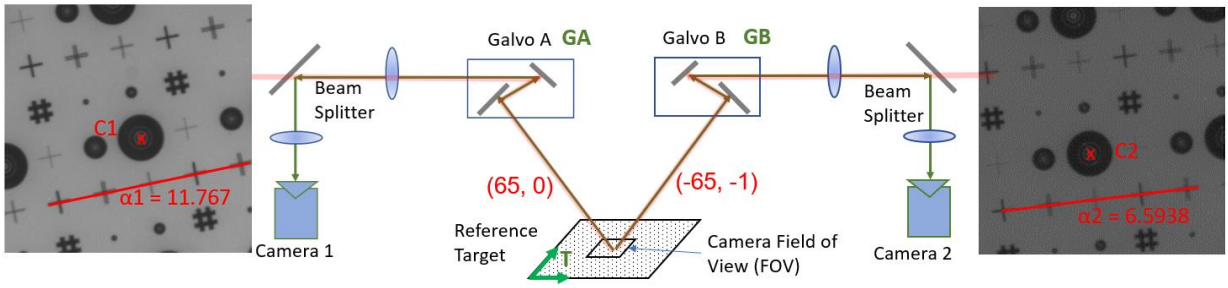

Figure 7. The figure illustrates dual laser calibration using an optical reference target. Both lasers are aligned to focus on the same position marker on the target.

The experimental process begins with a coaxial imaging setup, where a camera aligned with the processing laser captures images of the optical target as the galvo system scans it. The captured image positions, initially in the camera coordinate system, are then transformed to the target and galvo coordinate systems through a series of nonlinear and rotational transformations. This allows for the accurate calculation of positioning errors by comparing the commanded laser positions with the actual positions. To ensure the accuracy of these measurements, any optical distortions in the images are corrected through image alignment using a third-order polynomial transformation [9]. The actual scan path is then reconstructed by summing the interframe displacement vectors between consecutive images, allowing a detailed comparison between the reconstructed and commanded paths. Finally, the method includes an analysis of measurement uncertainties associated with image processing and alignment, demonstrating that the technique is robust and reliable within acceptable error margins.

Three sets of experiments were conducted (Table 2) using synchronized mode, where lasers A and B scanned simultaneously, and coaxial cameras A and B were triggered at the same time. In the first experiment, no compensation was applied except for the galvo position offsets. The compensation polynomial coefficients on the SAM controller were set to [0, 1, 65] for the X axis and [0, 1, 0] for the Y axis on Galvo A, and [0, 1, -65] for the X axis and [0, 1, -1.5] for the Y axis

on Galvo B (Figure 5, second order polynomial correction). In the second experiment, a second-order single-variable polynomial (poly2) was applied in the SAM controller for real-time compensation on each galvo axis. The third experiment utilized a third-order two-variable polynomial (poly33) to pre-compensate the build file, with real-time compensation in the SAM controller also applied. Detailed calibration results for each experiment are provided below.

Table 2. Experiment settings

Exp #	Galvo position correction type	Compensation	Command position	Measured position
1	No compensation applied except galvo position offset.	N/A	XYC	XYT_A1 XYT_B1
2	Real-time Poly2 compensation by SAM controller	Poly2	XYC	XYT_A2 XYT_B2
3	Real-time Poly2 compensation by SAM controller, and poly33 pre-compensation for the build file	Poly33	XYC	XYT_A3 XYT_B3

Experiment #1

This experiment begins with calibrations of the uncompensated system to establish a baseline for galvo accuracy. The same XYC command was used to scan Galvo A and Galvo B while simultaneously triggering Camera A and Camera B to capture images of the same optical reference. These images were then analyzed to obtain XYT_A1 and XYT_B1, the measured positions for Galvo A and B, respectively. The effectiveness of various compensation functions (*sf_t2c*), including poly33, poly22, poly11, poly3, poly2, and poly1, was compared by evaluating the compensation error obtained from *sf_t2c*(XYT_A1) – XYC. Figure 8 displays the compensation error plot for each function, while Figure 9 shows the coefficients of the compensation function for both Galvo A and Galvo B, obtained using a third-order polynomial (poly33) fit, each with 95% confidence bounds.

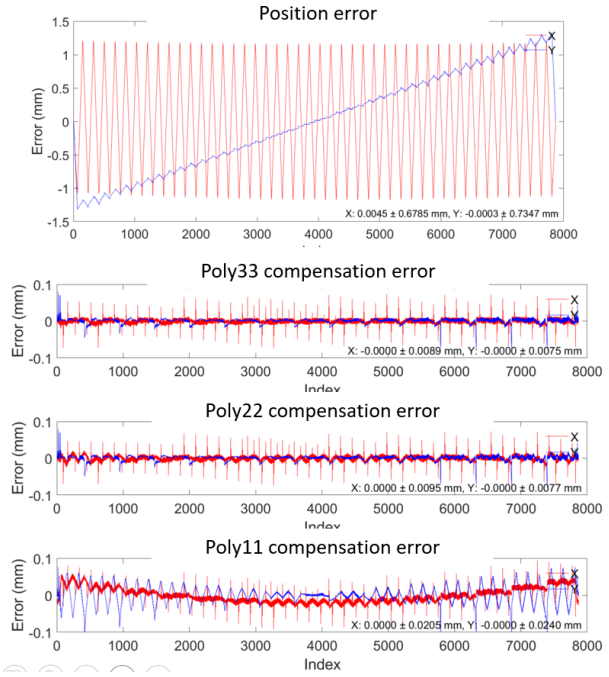

Model	MeanError_X	StdError_X	MeanError_Y	StdError_Y
No	0.004493	0.67852	-0.00027	0.734692
Poly33	**-1.75E-16**	**0.008864**	**-2.17E-15**	**0.007542**
Poly22	**3.44E-16**	**0.009523**	**-2.11E-15**	**0.007681**
Poly11	2.43E-16	0.020465	-2.17E-15	0.023992
Poly3	-8.26E-16	0.022489	8.33E-16	0.024117
Poly2	-8.79E-16	0.022489	-2.84E-15	0.024118
Poly1	-7.81E-16	0.022492	-7.01E-15	0.024139

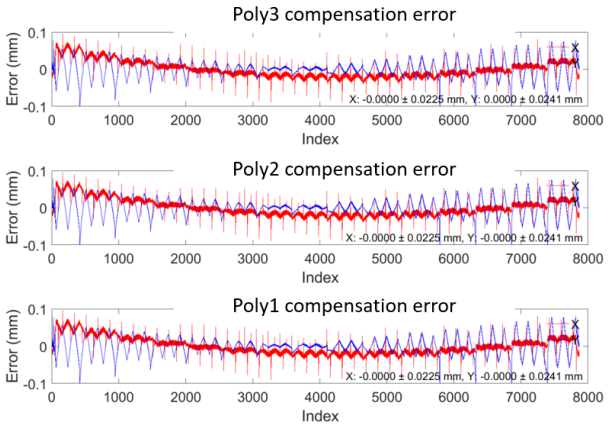

Figure 8. The comparison of compensation error for different polynomials. Position errors in the XY coordinates are measured by (XYT_A1 – XYC), and the compensation errors are calculated by *sf_t2c*(XYT_A1) – XYC. Errors in X (red) and Y (blue) coordinates are plotted separately.

Galvo A Calibration

- **X Calibration (sfx_t2c)**

```
sfx_t2c(x, y) = p00 + p10 * x + p01 * y + p20 *
x^2 + p11 * x * y + p02 * y^2 + p30 * x^3 + p21
* x^2 * y + p12 * x * y^2 + p03 * y^3
p00 = -0.001764 (-0.002147, -0.00138)
p10 = 0.9441 (0.9441, 0.9442)
p01 = -0.005919 (-0.005963, -0.005874)
p20 = -9.788e-06 (-1.125e-05, -8.328e-06)
p11 = -2.784e-06 (-4.078e-06, -1.49e-06)
p02 = 0.0001151 (0.0001137, 0.0001166)
p30 = 5.853e-08 (-7.392e-08, 1.91e-07)
p21 = 4.347e-09 (-1.112e-07, 1.199e-07)
p12 = 1.597e-06 (1.482e-06, 1.712e-06)
p03 = 9.749e-08 (-3.34e-08, 2.284e-07)
```

- **Y Calibration (sfy_t2c)**

```
sfy_t2c(x, y) = p00 + p10 * x + p01 * y + p20 *
x^2 + p11 * x * y + p02 * y^2 + p30 * x^3 + p21
* x^2 * y + p12 * x * y^2 + p03 * y^3
p00 = 0.001901 (0.00163, 0.002172)
p10 = 0.005184 (0.005153, 0.005216)
p01 = 0.9409 (0.9409, 0.9409)
p20 = -1.023e-06 (-2.057e-06, 1.001e-08)
p11 = -0.0001373 (-0.0001382, -0.0001364)
p02 = -5.639e-06 (-6.665e-06, -4.614e-06)
p30 = -1.81e-08 (-1.118e-07, 7.565e-08)
p21 = -7.703e-07 (-8.521e-07, -6.885e-07)
p12 = -7.763e-10 (-8.22e-08, 8.065e-08)
p03 = -1.709e-07 (-2.635e-07, -7.821e-08)
```

Galvo B Calibration

- **X Calibration (sfx_t2c)**

```
sfx_t2c(x, y) = p00 + p10 * x + p01 * y + p20 *
x^2 + p11 * x * y + p02 * y^2 + p30 * x^3 + p21
* x^2 * y + p12 * x * y^2 + p03 * y^3
p00 = 0.006555 (0.006232, 0.006878)
p10 = 0.9455 (0.9455, 0.9456)
p01 = 0.0006513 (0.0006136, 0.000689)
p20 = 3.392e-07 (-8.958e-07, 1.574e-06)
p11 = -8.788e-06 (-9.883e-06, -7.694e-06)
p02 = -0.0001196 (-0.0001208, -0.0001184)
p30 = 1.631e-07 (5.091e-08, 2.753e-07)
p21 = 8.166e-08 (-1.614e-08, 1.795e-07)
p12 = 1.864e-06 (1.767e-06, 1.961e-06)
p03 = -6.764e-08 (-1.784e-07, 4.308e-08)
```

- **Y Calibration (sfy_t2c)**

```
sfy_t2c(x, y) = p00 + p10 * x + p01 * y + p20 *
x^2 + p11 * x * y + p02 * y^2 + p30 * x^3 + p21
* x^2 * y + p12 * x * y^2 + p03 * y^3
p00 = 0.001232 (0.0009473, 0.001517)
p10 = 0.0001663 (0.0001329, 0.0001997)
p01 = 0.9418 (0.9417, 0.9418)
p20 = 3.476e-06 (2.387e-06, 4.564e-06)
p11 = 0.0001341 (0.0001331, 0.0001351)
p02 = -9.752e-06 (-1.083e-05, -8.673e-06)
p30 = 1.606e-08 (-8.284e-08, 1.15e-07)
p21 = -7.606e-07 (-8.468e-07, -6.744e-07)
p12 = 2.213e-07 (1.355e-07, 3.071e-07)
p03 = 2.299e-07 (1.323e-07, 3.275e-07)
```

Figure 9. The poly33 compensation functions for galvo A and galvo B respectively.

Experiment #2

This experiment tests the real-time compensation on the SAM controller. The compensation function is obtained by fitting a Poly2 to map XYT_A1 to (XYC + [65, 0]) for Galvo A and (XYT_B1 + position marker offset) to (XYC + [-65, -1]) for Galvo B. The position marker offset represents the difference in the positions of the same marker in images taken by Camera A and Camera B, and it is applied to align the origin of Galvo B with Galvo A. The resulting polynomials are shown in Figure 10a. Interestingly, for both Galvo A and B, the second-order coefficient is essentially 0 (accurate to four significant digits), consistent with the Poly33 coefficient fit shown in Figure 9.

The calibration coefficients were then programmed into the FPGA controller to enable real-time compensation. The effectiveness of this calibration was evaluated by repeating the calibration process, and the resulting position errors are shown in Figure 10b. The figure plots the Galvo A error XYC - XYT_A2, Galvo B error XYC - XYT_B2, and the difference between Galvo A and Galvo B (i.e., XYT_A2 - XYT_B2). The mean errors and standard deviations are also presented in Table 3. Interestingly, the errors appear to be out of phase with each other, suggesting that the poly2 calibration approach was insufficient. This finding aligns with the analysis in Figure 8, where all single-variable polynomials exhibited a similar compensation error pattern. To address this, Poly33 was fitted to map XYT_A2 and XYT_B2 to XYC, and the resulting polynomials were used to pre-compensate the build file for Experiment #3.

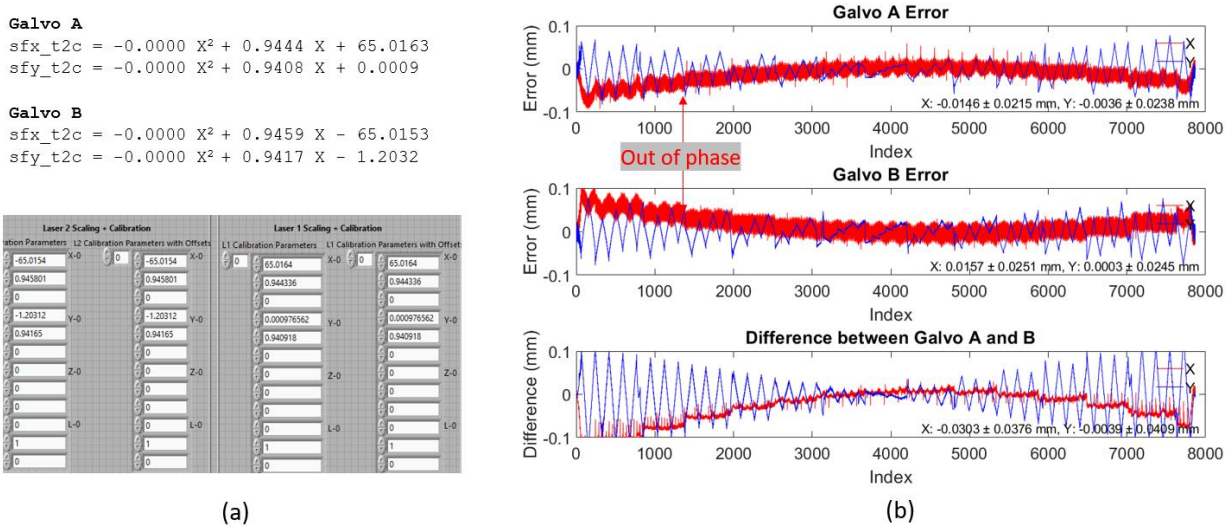

Figure 10. (a) The Poly2 compensation function and SAM controller input. (b) Position error from experiment #2. Errors in X (red) and Y (blue) coordinates are plotted separately.

Table 3. Mean and standard deviation (std) position error for Experiment #2

Average error	X-axis error (mean ± std) in μm	Y-axis error (mean ± std) in μm
Galvo A	-14.6 ± 21.5	-3.6 ± 23.8
Galvo B	15.7 ± 25.1	-0.3 ± 24.5
Galvo A – Galvo B	30.3 ± 37.6	3.9 ± 40.9

Experiment #3

This experiment demonstrates the effectiveness of Poly33 compensation, which requires pre-processing because the current SAM controller does not support real-time Poly33 compensation. Figure 11 shows the results for Experiment #3, with the average errors for Galvo A, Galvo B, and the difference between A and B presented in Table 4. The Galvo A error is calculated as XYC - XYT_A3, and the Galvo B error as XYC - XYT_B3. Upon examining the expanded plot, it can be observed that the X and Y errors oscillate around 0 by approximately ±20 µm, consistent with the image resolution of 20 µm/pixel. Interestingly, this oscillation is in phase for both galvos, resulting in a reduced error in the difference plot between Galvo A and Galvo B.

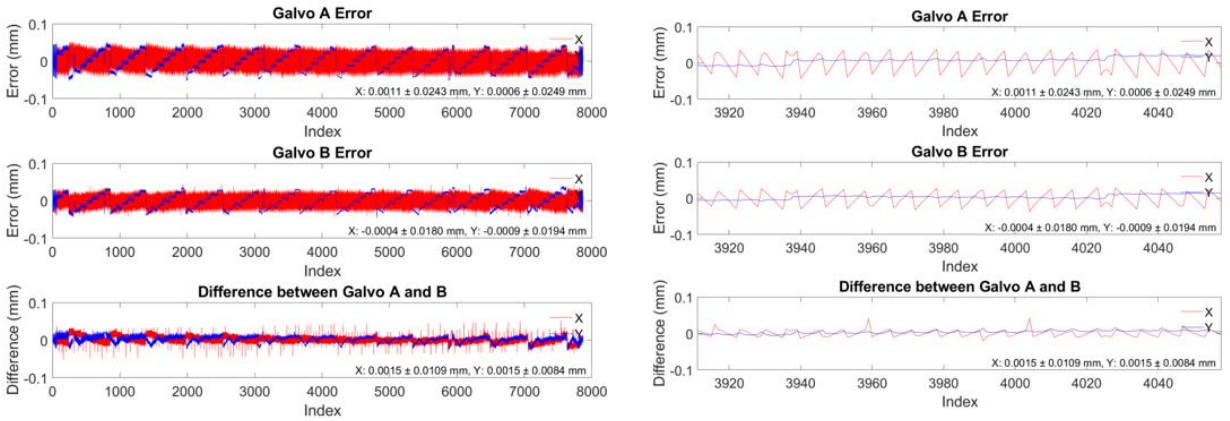

Figure 11. Position error for experiment #3. Right is an expanded view of the left.

Table 4. Mean and standard deviation (std) of compensation error for Experiment #3

Average error	X-axis error (mean ± std) in µm	Y-axis error (mean ± std) in µm
Galvo A	1.1 ± 24.3	0.6 ± 24.9
Galvo B	-0.4 ± 18.0	-0.9 ± 19.4
Galvo A – Galvo B	1.5 ± 10.9	1.5 ± 8.4

Discussion

The final calibration results from Experiment #3 showed that the poly33 pre-compensation model significantly reduced errors. For Galvo A, the error was reduced to (1.1 ± 24.3) µm in the X direction and (0.6 ± 24.9) µm in the Y direction, while for Galvo B, the error was (-0.4 ± 18.0) µm in the X direction and (-0.9 ± 19.4) µm in the Y direction. The difference between the two galvos was minimized to (1.5 ± 10.9) µm in the X direction and (1.5 ± 8.4) µm in the Y direction. These promising results demonstrate that our proposed calibration method can effectively compensate for errors in multi-laser systems.

One limitation identified in the study is the image resolution, which is approximately 20 µm per pixel. This relatively coarse resolution contributes to the larger uncertainty (standard deviation) observed in Experiment #3. As shown in Figure 11, the error pattern exhibits oscillations corresponding to the camera's pixel resolution, indicating that the camera's resolution imposes a fundamental limitation on the calibration accuracy. A higher-resolution camera could further enhance calibration precision by reducing this uncertainty.

The baseline calibration in Experiment #1 (Figure 8) provided valuable insights into the performance of different polynomial models for error compensation. Both the poly22 and poly33 models demonstrated effective compensation for galvo position errors. The position error plots from Figures 10 and 11, derived from experimental results (XYT – XYC), closely resemble the compensation error shown in Figure 8 (*sf_t2c*(XYT) – XYC), although the experimental position error show greater variance. This consistency suggests that the compensation algorithm itself is robust.

An interesting observation is that the differences between poly1, poly2, and poly3 compensations were minimal, indicating that higher-order terms in these models may not significantly contribute to error reduction. This suggests that cross-axis interference between the X and Y axes plays a role, and such interference cannot be compensated by poly11, implying that the issue is not merely a simple rotation or misalignment. Investigating the potential causes of this nonlinear cross-axis behavior, possibly related to the optical path involving a linear lens for laser spot size (focus position) adjustment and an F-theta lens, is beyond the scope of this study.

This study assumes that the laser's position aligns with the position marker. To achieve this, both the laser and the position marker need to be centered in the camera window. One method involves marking a cross with the laser and then adjusting the micro-stage (Figure 5) to center the cross in the camera window. The position marker can be centered by carefully offsetting the galvo. However, a more precise alternative is to use an up-looking camera to align the two lasers at the same point, similar to the laser spot size calibration method developed by Yeung et al [7]. The uncertainty in laser position measurement using the up-looking camera is primarily due to its 2.5 µm pixel resolution. Once the two lasers are aligned using the up-looking camera, the image offset procedure described in Figure 7 is no longer necessary. This approach will be demonstrated in future work.

While these compensations can be pre-processed before the scan, it makes more sense for the SAM controller to handle these errors in real-time, allowing the machine to be treated as inherently accurate. This approach simplifies scan file preparation and ensures consistent performance across different builds. The poly22 compensation appears to be the most suitable choice for this purpose, and enhancements incorporating this model will be considered for future versions.

The calibration process is straightforward and efficient. It involves placing an optical reference on the build plane, with the scanning and imaging process taking less than 2 minutes. The entire analysis process, from digital image correlation to generating the correction polynomials, is completed in under 30 minutes on a laptop computer. The calibration is not constrained by the size of the optical reference, as the corrections are applied through polynomials. However, using a larger optical reference may better handle non-uniform distortion. Fortunately, such optical references are very affordable. A key requirement is access to the coaxial camera and the ability to trigger it at designated scan locations.

Summary

A new in-situ laser calibration method for multi-laser L-PBF systems has been developed, offering a significant advancement in addressing the challenges associated with part quality at the stitched regions caused by misalignment between different lasers. The method leverages coaxial cameras aligned with the processing lasers to capture images during scanning, enabling precise, automated calibration of each laser to a global coordinate system without relying on external measurements. This in-situ approach allows for the collection of thousands of calibration points before the build process and ensures that the lasers are accurately aligned throughout the build.

This method has been implemented on the NIST AMMT 2.0 dual-laser system, where initial tests demonstrated promising results, reducing calibration errors to less than 20 µm. By ensuring precise alignment and synchronization of the laser beams, this technique holds potential for significantly improving the build quality of multi-laser L-PBF systems. The integration of this calibration method into the SAM controller presents both opportunities and challenges. While the poly22 model has proven effective for real-time error correction, further improvements are necessary to handle cross-axis interference and real-time processing limitations. Future work will explore the use of heating lasers and the application of higher-resolution cameras to enhance calibration accuracy further.

The study also highlights the potential for this method to support more advanced scan strategies, such as pre-sintering to reduce powder denudation, post-heating for residual stress relief, and creating specific heating conditions for microstructure control. These strategies, combined with the jerk-limited galvo control developed by NIST [10], could fully realize the advantages of multi-laser systems, enabling larger, faster builds with superior quality. Moving forward, the focus will be on refining the calibration process and further integrating it into the dual-laser control system, aiming to simplify scan file preparation while ensuring consistent and accurate performance across different builds. This method represents a crucial step in advancing the capabilities of multi-laser L-PBF systems and pushing the boundaries of additive manufacturing technology.

Reference

[1] Sing SL, Yeong WY. Laser powder bed fusion for metal additive manufacturing: perspectives on recent developments. Virtual and Physical Prototyping 2020;15:359–70. https://doi.org/10.1080/17452759.2020.1779999.

[2] Zhang C, Zhu H, Hu Z, Zhang L, Zeng X. A comparative study on single-laser and multi-laser selective laser melting AlSi10Mg: defects, microstructure and mechanical properties. Materials Science and Engineering: A 2019;746:416–23. https://doi.org/10.1016/j.msea.2019.01.024.

[3] Yin J, Wang D, Wei H, Yang L, Ke L, Hu M, et al. Dual-beam laser-matter interaction at overlap region during multi-laser powder bed fusion manufacturing. Additive Manufacturing 2021;46:102178. https://doi.org/10.1016/j.addma.2021.102178.

[4] Heeling T, Zimmermann L, Wegener K (2016) Multi-beam strategies for the optimization of the selective laser melting process. In: proceedings of the 27th annual international solid freeform fabrication symposium, The University of Texas at Austin, US n.d.

[5] Land WS. Effective calibration and implementation of galvanometer scanners as applied to direct metal laser sintering, 2014.
[6] Lu Y, Badarinath R, Lehtihet EA, De Meter EC, Simpson TW. Experimental sampling of the Z-axis error and laser positioning error of an EOSINT M280 DMLS machine. Additive Manufacturing 2018;21:501–16. https://doi.org/10.1016/j.addma.2018.03.029.
[7] Yeung H, Grantham S. Laser Calibration for Powder Bed Fusion Additive Manufacturing Process. Solid Freeform Fabrication Symposium 2022, Austin, TX, US n.d.
[8] Zhong Q, Tian X-Y, Huang X-K, Tong Z-Q, Cao Y, Li D-C. High-accuracy calibration for multi-laser powder bed fusion via in situ detection and parameter identification. Adv Manuf 2022;10:556–70. https://doi.org/10.1007/s40436-022-00392-3.
[9] Yeung H, Lane BM, Donmez MA, Moylan S. In-situ calibration of laser/galvo scanning system using dimensional reference artefacts. CIRP Annals 2020:S0007850620300160. https://doi.org/10.1016/j.cirp.2020.03.016.
[10] Yeung H, Lane BM, Donmez MA, Fox JC, Neira J. Implementation of Advanced Laser Control Strategies for Powder Bed Fusion Systems. Procedia Manufacturing 2018;26:871–9. https://doi.org/10.1016/j.promfg.2018.07.112.
[11] Shi R, Khairallah SA, Roehling TT, Heo TW, McKeown JT, Matthews MJ. Microstructural control in metal laser powder bed fusion additive manufacturing using laser beam shaping strategy. Acta Materialia 2020;184:284–305. https://doi.org/10.1016/j.actamat.2019.11.053.
[12] Yeung H. Methodologies and Implementation of Laser Powder-Bed Fusion Process Control. ASM Handbook Volume 24A: Additive Manufacturing Design and Applications, ASM International; 2023, p. 1–9. https://doi.org/10.31399/asm.hb.v24A.a0006955.